Journal of Materials Chemistry A

PAPER

View Article Online
View Journal | View Issue

Cite this: J. Mater. Chem. A, 2015, 3, 3480

A high-rate aqueous symmetric pseudocapacitor based on highly graphitized onion-like carbon/birnessite-type manganese oxide nanohybrids†

Katlego Makgopa,[a] Paul M. Ejikeme,[a] Charl J. Jafta,[b] Kumar Raju,[b] Marco Zeiger,[cd] Volker Presser*[cd] and Kenneth I. Ozoemena*[ab]

Received 7th December 2014
Accepted 15th December 2014

DOI: 10.1039/c4ta06715k

www.rsc.org/MaterialsA

We present a study on the pseudocapacitive properties of birnessite-type MnO_2 grafted on highly graphitized onion-like carbon (OLC/MnO_2). In a three-electrode setup, we evaluated two different substrates, namely a platinum disc and nickel foam. The OLC/MnO_2 nanohybrid exhibited a large specific capacitance (C_{sp}) of 295 and 323 F g^{-1} (at 1 A g^{-1}) for the Pt disc and Ni foam, respectively. In addition, the Ni foam substrate exhibited much higher rate capability (power density) than the Pt disc. A symmetrical two-electrode device, fabricated with the Ni foam, showed a large C_{sp} of 254 F g^{-1}, a specific energy density of 5.6 W h kg^{-1}, and a high power density of 74.8 kW kg^{-1}. These values have been the highest for onion-based electrodes so far. The device showed excellent capacity retention when subjected to voltage-holding (floating) experiments for 50 h. In addition, the device showed a very short time constant (τ = 40 ms). This high rate handling ability of the OLC/MnO_2 nanohybrid, compared to literature reports, promises new opportunities for the development of aqueous-based pseudocapacitors.

Introduction

Supercapacitors are advanced systems for electrochemical energy storage.[1,2] Two different types of supercapacitors can be differentiated: (a) electrical double-layer capacitors (EDLCs) that only rely on charge storage *via* ion electrosorption in an electrical double-layer, and (b) pseudocapacitors that utilize fast (surface) redox reactions.[3–6] Over the last years, supercapacitors have attracted tremendous attention due to their excellent properties such as high power density, long cycle ability, high efficiency, and relying on abundantly available carbon materials.[7,8] Considering energy and power performance, supercapacitors play a key role as intermediates between batteries and electrolytic capacitors[9] and find widespread applications for fast charge–discharge and uninterrupted power supply applications as well as in combination with batteries in hybrid systems.[10] There have been extensive studies of varieties of carbon materials for supercapacitor electrodes because of their large specific surface area (SSA), high conductivity, facile availability, and chemical stability.[5,11] Some of the best performing carbon materials include activated carbon,[12] carbon nanotubes (CNTs),[13] graphene,[14,15] carbon nanofibers (CNFs),[16,17] and carbon aerogels.[18]

Among carbon nanomaterials, non-porous carbon onions, also known as onion-like carbon (OLC), have attracted major research interest as electrode materials for energy storage, for example, advanced anode electrodes for lithium ion batteries,[19,20] pseudocapacitors,[21,22] and ultrahigh-power electrical double-layer capacitors.[23–25] The major attractions stem from the ability to prepare them on a large scale by thermal annealing of nanodiamonds and the superior power handling ability.[26] OLCs are described as multi-shell fullerenes[27] that, unlike fullerenes, exhibit a high electrical conductivity commonly in the range of 2–4 S cm^{-1}.[25] However, the limited surface area of OLCs (200–600 m^2 g^{-1}) has also resulted in limited double-layer capacitance (usually between 25 and 50 F g^{-1}, equivalent up to 2 W h kg^{-1} at 1 V).[25,26]

OLCs derived from thermal treatment of nanodiamonds (NDs)[28] are highly graphitic spherical particles (5–10 nm) that consist of several concentric carbon shells.[29] Alternative synthesis methods may also yield larger OLCs with diameters of more than 10 nm (ref. 19 and 30) and include condensation of carbon vapor[31] or electron beam irradiation.[32] However, thermal annealing of NDs[33] at temperatures between 1000 and 2000 °C is currently the preferred technique to synthesize OLCs since large amounts of material can be obtained per run.[34] Also, a narrow size distribution of the ND precursor translates into a narrow size distribution of the resulting onion-like carbons.[21]

[a]Department of Chemistry, University of Pretoria, Pretoria 0002, South Africa. E-mail: kozoemena@csir.co.za; Fax: +27-128412135; Tel: +27-128413664

[b]Energy Materials, Materials Science and Manufacturing, Council for Scientific & Industrial Research (CSIR), Pretoria 0001, South Africa

[c]INM-Leibniz Institute for New Materials, 66123 Saarbrücken, Germany. E-mail: volker.presser@inm-gmbh.de; Fax: +49-6819300223; Tel: +49-6819300177

[d]Saarland University, 66123 Saarbrücken, Germany

† Electronic supplementary information (ESI) available. See DOI: 10.1039/c4ta06715k

Birnessite-type MnO_2 (in this paper referred to as just "MnO_2") exhibits a two-dimensional layered structure (see ESI, Fig. S1†) displaying edge-sharing MnO_6 octahedra in the sheets and metal cations (for example K^+) and water molecules in the interlayer region. Hence, an appropriate chemical representation would be $K_xMn_2O_4 \cdot yH_2O$ (with $x \leq 0.5$ and $y \leq 1.5$).[35] This metal oxide has become an attractive electrode material for efficient and low-cost development of supercapacitors due to its natural abundance and environmental compatibility.[36–42] However, because of its low electrical conductivity (10^{-6} to 10^{-5} S cm^{-1}) and poor power handling capability, the electrochemical performance of MnO_2 electrodes is rather low, which significantly limits its potential applications as high-power supercapacitor electrodes.[43] The capacitive performance, redox activity, as well as utilization of MnO_2 can be enhanced by the addition of conductive materials.[44–46] However, the resulting performance strongly depends on the quality and properties of such carbon/metal oxide hybrid materials.

This work, for the first time, reports the electrochemistry of MnO_2 integrated with highly graphitized OLCs derived from NDs (herein abbreviated simply as OLC/MnO_2 nanohybrid) as a high-power pseudocapacitor in a neutral aqueous medium (1 M Na_2SO_4). Previous studies related to MnO_2 with "carbon onions" were carried out using low-graphitized materials obtained from either clarified butter ("Ghee")[30] or phenolic-formaldehyde resins with much larger particle diameters (tens of nm).[42] Whilst these initial reports are encouraging, we show in this study that by using highly graphitized OLCs, OLC/MnO_2 nanohybrids exhibit a very high power density (~75 kW kg^{-1}). In addition, our devices show excellent capacitance retention upon long-hour voltage-holding and very low equivalent distribution resistance (EDR ≈ 3 Ω cm^2) with a response time of just a few milliseconds.

Experimental section

Precursor and synthesis of OLC and OLC/MnO_2

OLC was synthesized from nanodiamond (ND) powder with a purity of 98–99% (NaBond Technologies) and thoroughly characterized as recently described.[47] Briefly, ND powder was placed in a closed-lid cylindrical graphite crucible (30 mm in diameter and 20 mm in height) and thermally annealed in a water-cooled high temperature vacuum furnace with tungsten heaters (Model: 1100-3580-W1, Thermal Technology Inc.). The heating and cooling rates were both 15 °C min^{-1} and the chamber pressure ranged between 10 and 100 mPa. The final OLC was annealed at 1750 °C for 3 h. The OLC/MnO_2 nanohybrid material was prepared using the conventional hydrothermal reduction technique. Typically, 40 mg of OLC was dispersed by sonication in 30 mL of 0.02 M $KMnO_4$ (Merck), and the mixture (pH = 7.05) was refluxed at 130 °C in an oil bath for 24 h with continuous magnetic stirring. The resultant dispersion was then centrifuged and washed several times with deionized water, and finally dried at 60 °C overnight in a vacuum oven. All chemicals were of analytical grade and used as received. Deionized water was used throughout the synthesis process.

Structural characterization

Surface morphology characterization of the samples was obtained using a JSM-7500F (JEOL, Japan) scanning electron microscope (SEM) operated at 3.0 kV. Energy dispersive X-ray spectra (EDX) were recorded with an EDX system (Oxford Instruments) at 5 different positions. The chemical composition was calculated using the AZtec energy analysis software (Oxford Instruments). Transmission electron microscopy (TEM) samples were prepared by dispersing powders in ethanol and placing the dispersion over a copper grid with a lacey carbon film. All measurements were carried out with a 2100F microscope (JEOL) operating at 200 kV. X-ray diffraction (XRD) patterns of the samples were collected using an X'Pert-Pro MPD diffractometer (PANalytical) with theta/theta geometry (step width: 0.0263° s^{-1}), operating a copper tube at 40 kV and 40 mA. The instrumental resolution function was characterized with the NIST SRM 660a (LaB_6) standard. The patterns were recorded in the range of 5–148° 2θ. Qualitative phase analysis of the samples was conducted using Bruker EVA software using the PDF database.

Raman spectra were recorded with a Renishaw inVia Raman microscope using a Nd-YAG laser with an excitation wavelength of 532 nm and a grating with 1800 lines mm^{-1} yielding a spectral resolution of *ca.* 1.2 cm^{-1}. The spot size on the sample was in the focal plane *ca.* 2 μm using an output power of 0.5 mW. Spectra were recorded for 30 s and accumulated 50 times to eliminate cosmic rays and to obtain a high signal-to-noise and signal-to-background ratio. Peak fitting was achieved by employing Lorentzian peaks assuming four components for the carbon spectrum between 1000 and 1800 cm^{-1}. Fourier infrared spectroscopy (FTIR) analyses were carried out using a Perkin Elmer FT-IR spectrophotometer. OLC and OLC/MnO_2 nanohybrids were analyzed as KBr pellets (10 scans).

X-ray photoelectron spectroscopy (XPS) experiments were carried out on a Kratos Axis Ultra-DLD system (Shimadzu) with monochromated Al Kα radiation (1486.6 eV). Binding energies were calibrated using the containment carbon (C 1s at 284.6 eV). The spectra analysis was performed with the XPS Peak 4.1 program and a Shirley function was used to subtract the background. The metal oxide content in the nanohybrid was determined by thermogravimetric analysis (TGA) using an STA Jupiter 449 C (Netzsch) in an Ar/O_2 atmosphere at a temperature scan rate of 10 K min^{-1}.

Nitrogen gas sorption measurements were made with a Quantachrome Autosorb iQ system. The samples were outgassed at 150 °C for 10 h under vacuum conditions. Gas sorption was performed in liquid nitrogen (−196 °C) with a relative pressure range of 10^{-7} to 0.95 in 68 steps. The specific surface area (SSA) was calculated with the ASQwin-software using the Brunauer–Emmett–Teller (BET) equation[48] in the relative pressure range of 0.01–0.2. We also calculated the SSA and pore size distribution (PSD) *via* quenched-solid density functional theory (QSDFT)[49] with a hybrid model for slit and cylindrical pores and pore size between 0.56 and 37.5 nm.

Electrochemical characterization

All electrochemical measurements were carried out using a Bio-Logic VMP 300 potentiostat/galvanostat using either a three-electrode (half-cell) or a two-electrode (full cell) configuration. For the three-electrode configuration a Pt disc and nickel foam were used as substrates for the working electrodes. For the three-electrode configuration using a Pt disc, a custom-built three-electrode cell (*cf.* ref. 47) was used. The working electrode was prepared by drop-casting 7.1 mg mL^{-1} OLC colloidal dispersion (10 mass% polyvinylidenfluoride, PVDF in ethanol) or 9.0 mg mL^{-1} OLC/MnO_2 nanohybrid colloidal dispersion (in anhydrous *N*-methyl-2-pyrrolidone, NMP) onto a Pt disc (diameter: 12 mm, thickness: 100 μm, purity 99.99%, Carl Schaefer) and dried at 80 °C overnight in a vacuum oven at 20 mbar to remove the solvent. Polytetrafluoroethylene (PTFE) bound (5% in total electrode mass) activated carbon (YP50F, Kuraray Chemical) served as a counter electrode and was largely oversized in charge capacity as compared to the working electrode. A platinum wire (diameter 1 mm, purity 99.99%, Carl Schaefer) served as a pseudo-reference electrode. For the nickel foam based three-electrode configuration, the nickel foam (Celmet: thickness = 1.6 mm, surface area = 7500 m^2 m^{-3}, cell size = 0.5 mm, 48–52 cells per inch) was cleaned prior to use, in a 1 M HCl solution, washed with a copious amount of de-ionized water to a neutral pH, and dried under vacuum. It was pasted with a mixture of OLC/MnO_2 nanohybrid, carbon black (CB, Degussa), and polyvinylidene fluoride (PVDF) (mass% of 80 : 15 : 5 respectively, homogeneously mixed with a few drops of anhydrous *N*-methyl-2-pyrrolidone using a paste pestle and mortar). The CB and PVDF served as a conductive additive and a binder, respectively. The electrode was then dried at 80 °C overnight in a vacuum oven, and pressed to a thickness of 250 μm. The electrode was cut into a piece of 1 cm × 1 cm, while the mass loading was typically 1 mg cm^{-2} for the Pt disc and nickel foam. An oversized glassy carbon plate (1.6 × 1.6 cm^2) was used as the counter electrode and Ag/AgCl (3 M KCl) as the reference electrode. The two-electrode configuration used the nickel foam as substrate. Both the positive and negative electrodes used nickel foam coated with the OLC/MnO_2 nanohybrid, obtained as described for the three-electrode above. The resulting slurry was coated onto the nickel foam substrate (~3 cm^2) with a spatula using an average mass loading of 1 mg cm^{-2}. Symmetric cells were also prepared using nickel foam loaded with only OLC. In all experiments, 1 M Na_2SO_4 was used as the electrolyte and a porous glass fiber (Whatman Grade GF/D Glass Microfiber Filters, Sigma-Aldrich) served as the separator. For the three-electrode configuration, cyclic voltammetry was performed at various scan rates (2–100 mV s^{-1}). Voltage-holding (floating) experiments were performed for 10 h at 0.8 V, then galvanostatically charged–discharged between 0.0 and 0.8 V at 1 A g^{-1}, repeating the process five times (*i.e.*, a total of 50 h). Electrochemical impedance spectroscopy (EIS) data were obtained between 100 kHz and 10 mHz with a perturbation amplitude (rms value) of the AC signal of 2 mV. Every EIS experiment was performed after allowing the cell to equilibrate for 5 min at the chosen fixed potential.

The specific capacitance (C_{sp}) of the half-cells, obtained from CV and galvanostatic discharge curves, was evaluated using the established equations (1) and (2), respectively.

$$C_{sp}\left(\mathrm{F\ g^{-1}}\right) = \frac{\int i\mathrm{d}t}{\Delta V m} \quad (1)$$

$$C_{sp}\left(\mathrm{F\ g^{-1}}\right) = \frac{i\Delta t}{\Delta V m} \quad (2)$$

where i (A) is the current, ΔV (V)/Δt (s) the slope of the discharge curve, and m (g) the mass of the active electrode, and V (V) is the voltage obtained during charge. Note that the iR drop ranged from 3.2 to 1.1 Ω at current densities of 0.1–10 A g^{-1}.

The specific capacitance (C_{sp}), maximum specific power density (P_{max}) and specific energy density (E_{sp}) for the full cells (symmetric devices) were evaluated from the slope of the charge–discharge curves using eqn (3)–(6).[1]

$$C(\mathrm{F}) = \frac{i}{\Delta V/\Delta t} \quad (3)$$

$$C_{sp}\left(\mathrm{F\ g^{-1}}\right) = \frac{4C}{m} \quad (4)$$

$$P_{max}\left(10^3\ \mathrm{W\ kg^{-1}}\right) = \frac{V^2}{4mR_s} \quad (5)$$

$$E\left(\frac{1}{3.6}\ \mathrm{Wh\ kg^{-1}}\right) = \frac{CV^2}{2m} \quad (6)$$

where i (A) is the applied current, ΔV (V)/Δt (s) the slope of the discharge curve and m (g) the total mass of both electrodes, C (F) the calculated capacitance, V (V) is the maximum voltage obtained during charge, and R_s is the equivalent series resistance (ESR).

Results and discussion

SEM, TEM, and gas sorption analysis

The surface morphologies of OLC and the OLC/MnO_2 nanohybrid studied using SEM are shown in Fig. 1a and c and using TEM in Fig. 1b and d. The primary particle size of carbon onions is in the range of a few nanometers as seen from the TEM images in agreement with our previous findings.[47] This primary particle size is maintained for the OLC/MnO_2 nanohybrid. Compared with OLC, OLC/MnO_2 hybrid nanoparticles exhibited an obviously different morphology. The selected area electron diffraction (SAED) pattern in the inset of Fig. 1d shows lattice fringes for crystalline MnO_2 and circular lattice shells for OLC.[30] Rather than a monolayer or multilayer coating of each carbon onion, an effective OLC/MnO_2 nanohybrid was obtained with nanodomains of highly mixed graphitic carbon and metal oxide. The amount of metal oxide was determined by TGA to represent 47 mass% of the OLC/MnO_2 nanohybrid material (see ESI, Fig. S2†). Also, the TGA data show the excellent thermal stability of OLC with an onset of oxidation at around 630 °C as a result of the highly graphitic character of carbon onions synthesized at 1750 °C.

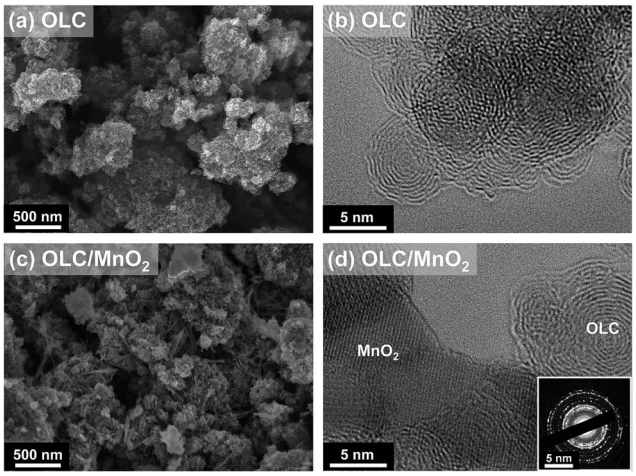

Fig. 1 SEM images of (a) OLC and (c) the OLC/MnO_2 nanohybrid; TEM images of (b) OLC and (d) the OLC/MnO_2 nanohybrid. The inset is the corresponding SAED pattern of (d).

Fig. 2 shows nitrogen gas sorption data for OLC and the OLC/MnO_2 nanohybrid. As we see, OLC/MnO_2 exhibits a QSDFT SSA of 122 $m^2\ g^{-1}$ with a distribution of micropores (<2 nm) and mesopores (between 2 and 50 nm). This represents a severe loss in the specific surface area compared to OLC with a QSDFT SSA of 391 $m^2\ g^{-1}$ and is mostly related to the higher molecular mass and higher density of MnO_2 in addition to pore blocking.[50] Yet, Fig. 2b shows that the overall pore size distribution is preserved after the addition of MnO_2 at a lower total pore volume.

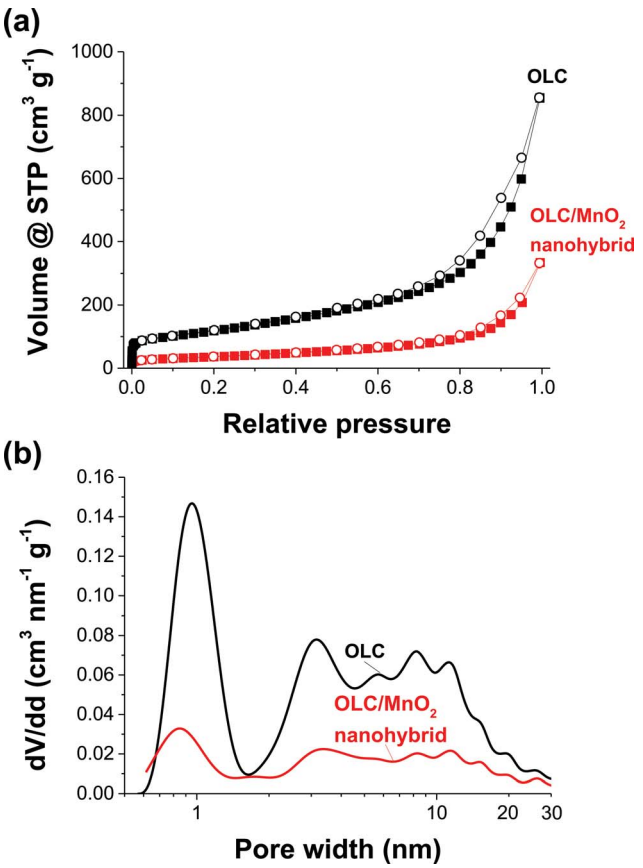

Fig. 2 (a) Nitrogen adsorption–desorption isotherms at −196 °C and (b) QSDFT pore size distribution overlays of OLC and the OLC/MnO_2 nanohybrid.

XRD, Raman, FTIR, EDX, and XPS studies

Fig. 3 illustrates the Raman spectra, X-ray diffraction patterns, and FTIR spectra of OLC and the corresponding OLC/MnO_2 nanohybrid material. The presence of MnO_2 is confirmed by a strong Raman signal at around 565 cm^{-1},[51] (Fig. 3a). The presence of the OLC in the hybrid from the XRD analysis is confirmed by Raman peaks associated with the carbon D-mode (1350 cm^{-1}) and G-mode (1590 cm^{-1}) of OLC/MnO_2. Peak analysis (Fig. 3a) shows that the hydrothermal synthesis only insignificantly changes the OLC structure: both the D- and G-mode remain almost unchanged. In particular, the I_D/I_G ratios before and after MnO_2 deposition are almost identical to the values of 1.20 and 1.25, respectively. The FWHM values for both the D-mode and the G-mode were measured to be 73.1 cm^{-1} and 69.8 cm^{-1} before the deposition and to be 78.5 cm^{-1} and 65.4 cm^{-1} after the MnO_2 deposition. The only minor change related to the carbon signal is identified at around 1100 to 1200 cm^{-1} which may indicate the formation of a small amount of functionalized carbon.[52] FTIR was used to study further the electrode materials as shown by Fig. 3c. The well pronounced peak at 550 cm^{-1} is due to the Mn–O–Mn asymmetric stretching vibration. The broad peak at 3450 cm^{-1} is assigned to hydroxyl groups which suggests that there are water molecules in the interlayers (see also the structure given in the ESI, Fig. S1†).[53]

From the XRD patterns of the OLC/MnO_2 nanohybrid (Fig. 3b), the peak at around 26° 2θ is associated with the (002) plane of graphitic carbon and it can be observed also in OLC/MnO_2 diffractograms indicating the presence of carbon in the nanohybrid. The other peaks can be indexed to birnessite-type MnO_2 (PDF 42-1317). All diffraction peaks of the metal oxide are broadened which indicates the nanocrystalline nature of the MnO_2 with an average coherence length (domain size) in the range of 5–10 nm. The calculated carbon *d*-spacing for the (002) plane is 0.352 nm and remains at that value with or without the presence of MnO_2. This represents a small increase in lattice spacing compared to an ideal graphite crystal (*i.e.*, 0.344 nm) as is well-known for the carbon onion structure.[52]

Chemical analysis confirms the presence of birnessite, meaning, not of pure MnO_2 but of a material following the average formula $K_xMn_2O_4 \cdot yH_2O$. Semi-quantitative analysis of OLC EDX spectra (Fig. 4a and Table 1) shows less than 0.2 mass% of impurities alongside *ca.* 9 mass% of surface oxygen. The metal oxide shows an average molar Mn : K ratio of 4.6 : 1 which is somewhat larger than the maximum stoichiometric value of 4 : 1. The small difference might indicate the presence of minor amounts of residual $KMnO_4$. Yet, we note that the previously reported non-carbon content of around 47 mass% is in agreement with our EDX data (54.3 mass%).

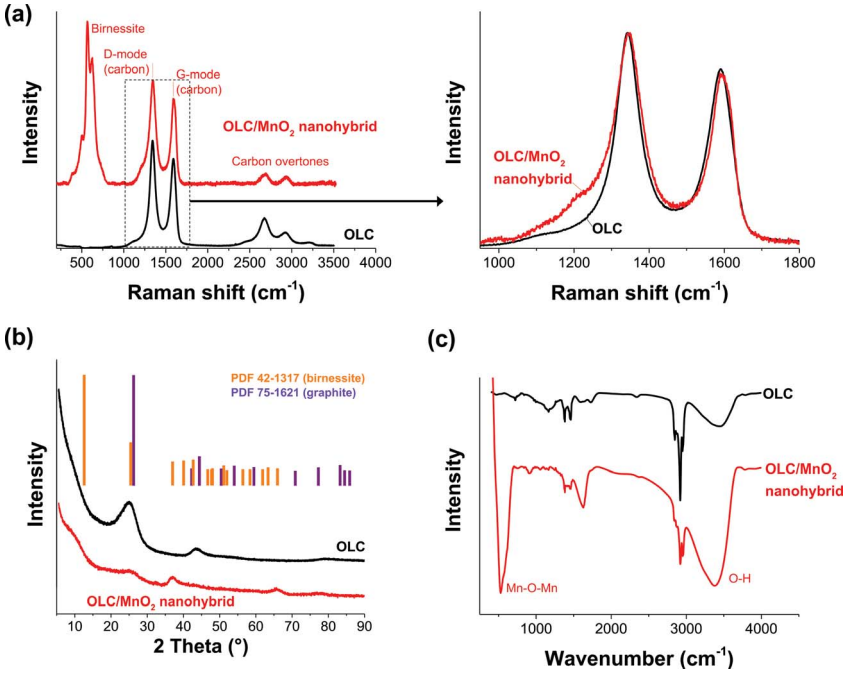

Fig. 3 (a) Raman spectra, (b) X-ray diffraction pattern, and (c) FTIR spectra of OLC and the OLC/MnO_2 nanohybrid.

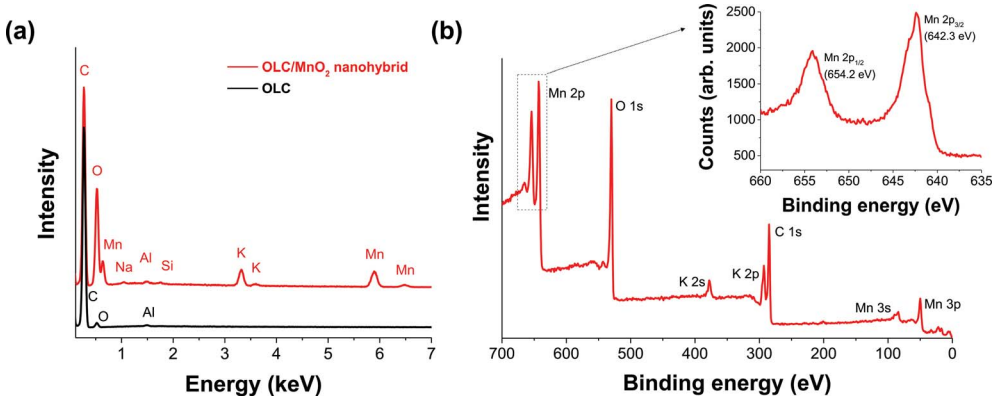

Fig. 4 (a) Energy dispersive X-ray (EDX) spectra of OLC and the OLC/MnO_2 nanohybrid and (b) X-ray photoelectron spectrum (XPS) of the OLC/MnO_2 nanohybrid.

Only minor impurities of Si and Na can be detected which stem from impurities in the $KMnO_4$. XPS analysis of OLC/MnO_2 (Fig. 4b) shows the binding energy peaks of Mn and C. The Mn 2p region consisted of a spin–orbit doublet with Mn $2p_{1/2}$ and Mn $2p_{3/2}$ having binding energies of 654.2 eV and 642.3 eV, respectively.[54] The energy separation between Mn $2p_{1/2}$ and Mn $2p_{3/2}$ of 11.9 eV is an indication of Mn in a +4 oxidation state.[55–57] From the XPS survey scan, we also see the presence of significant amounts of K in addition to Mn, C, and O.

Comparative performance of half-cells with Pt disc or Ni foam

Fig. 5 and 6 compare the electrochemical performance of the three-electrode configurations using either a platinum disc (Fig. 5) or nickel foam (Fig. 6) as current collectors. The CV curves of OLC (Fig. 5a) are characteristic of double-layer capacitive materials, while the CV curve of the OLC/MnO_2 nanohybrid shows redox-peaks indicative of faradaic reactions (Fig. 6a). The same conclusions can be drawn from the galvanostatic charge–discharge profiles (Fig. 5b and c *vs.* Fig. 6b and c).[58,59] We also see a high power handling ability of the materials with a comparatively small drop in the specific capacitance of OLC/MnO_2 (335–180 F g^{-1}) as a function of the current density (0.3–32 A g^{-1}), Fig. 6d.

The key findings from Fig. 5 and 6 may be summarized as follows: (i) the specific capacitance of OLC/MnO_2 is more than a magnitude higher than that of OLC for both current collectors (*i.e.*, Ni foam and a Pt disc); (ii) both types of current collectors gave an essentially similar specific capacitance at different current densities (*e.g.*, 250 F g^{-1} at 5 A g^{-1}); and (iii) the stable voltage window for the Pt disc is narrower (0–0.5 V) than that of

Table 1 Chemical composition of OLC and the OLC/MnO_2 nanohybrid measured by EDX in mass% and atom%

(Mass%)	C	O	Na	Al	Si	K	Mn
OLC	90.8 ± 1.7	9.1 ± 1.7	—	0.2 ± 0.1	—	—	—
OLC/MnO_2	45.7 ± 1.4	20.3 ± 1.9	0.2 ± 0.1	0.3 ± 0.1	0.2 ± 0.1	4.5 ± 1.2	28.9 ± 2.6
(Atom%)	C	O	Na	Al	Si	K	Mn
OLC	93.0 ± 1.3	7.0 ± 1.3	—	0.1 ± 0.1	—	—	—
OLC/MnO_2	66.3 ± 1.5	22.1 ± 1.7	0.1 ± 0.1	0.2 ± 0.1	0.1 ± 0.1	2.0 ± 0.6	9.2 ± 1.0

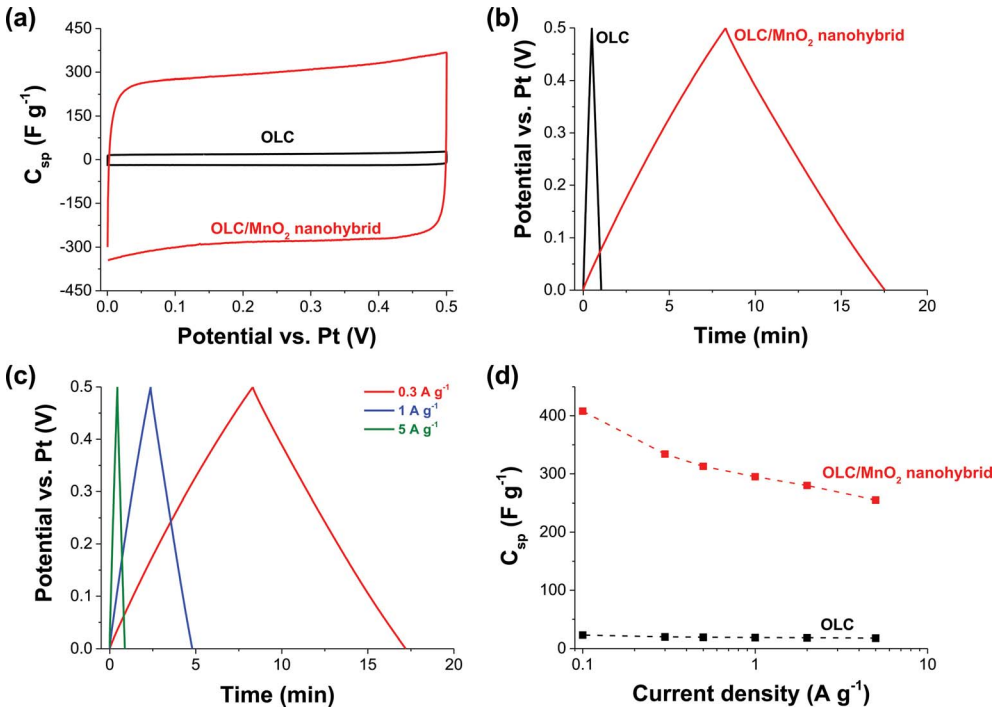

Fig. 5 3-electrode configuration with a Pt disc as the current collector: (a) cyclic voltammograms at 2 mV s^{-1}, (b) galvanostatic charge–discharge curves at 0.3 A g^{-1} comparing OLC and the OLC/MnO_2 nanohybrid, (c) galvanostatic charge–discharge curves for the OLC/MnO_2 nanohybrid at various current densities, and (d) Csp *vs.* current densities of the OLC/MnO_2 nanohybrid. Electrolyte: aqueous 1 M Na_2SO_4.

the nickel foam (0–1.0 V). The nickel foam alone only insignificantly contributes to the charge storage mechanism (see ESI, Fig. S3†). We also note that carbon onions alone, that is without the presence of MnO_2, only exhibit a low specific capacitance of 12 F g^{-1}.

As summarized in Table 2, the maximum C_{sp} values for our 3-electrode tests (335–408 F g^{-1} between 0.1 and 0.3 A g^{-1}) are much higher than those recorded in the literature. The impressive value (603 F g^{-1} at 10 A g^{-1}) for electrodeposited MnO_2-nanopillars reported by Yu *et al.*[73] for their flexible nanostructured electrode obtained by combined sputter-coating and electrodeposition (PAN/Au–Pd/MnO_2, *i.e.*, comprised of a cocktail of polyacrylonitrile polymer and very expensive precious metals of palladium and gold) may, amongst other factors, be related to the thin film nature of their system and the mass of active materials used in their calculations. Our values are somewhat comparable to those of the recent work by Ruoff *et al.*[39] involving the elaborate preparation of mesoporous nanotubes assembled from interwoven ultrathin birnessite-type MnO_2 nanosheets. Note that our result is much higher than that of the "OLC"/MnO_2 (~190 F g^{-1} at 0.2 A g^{-1}) reported by Wang *et al.*,[42] and the disparity can be related to the high graphitization of our OLC.

Symmetric pseudocapacitor with a nickel foam substrate

Further investigation of the OLC and OLC/MnO_2 as a full cell symmetric supercapacitor was carried out using nickel foam as the current collector considering its lower cost and better performance at half-cell experiments compared to platinum. Fig. 7 shows CVs (Fig. 7a and c) and galvanostatic charge–discharge curves (Fig. 7b and d) of the OLC and OLC/MnO_2 nanohybrid. In agreement with the three-electrode experiment, two-electrode data of the OLC/MnO_2 nanohybrid show much higher gravimetric capacitance compared to OLC electrodes.

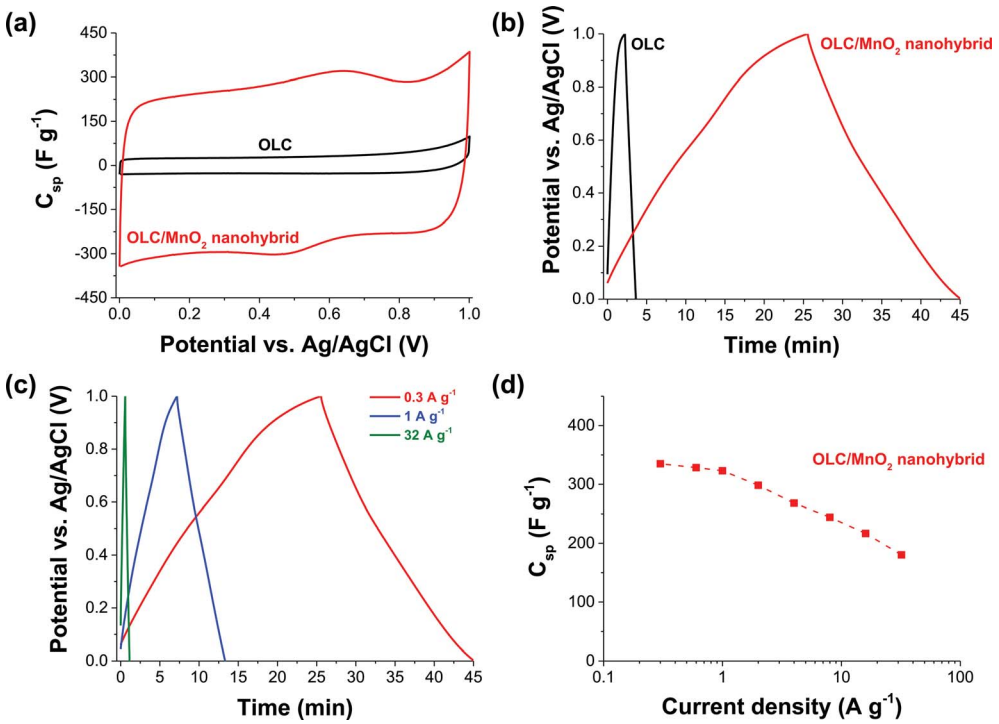

Fig. 6 3-electrode configuration with nickel foam as the current collector: (a) cyclic voltammograms at 5 mV s^{-1} and (b) galvanostatic charge–discharge curves at 0.3 A g^{-1} comparing OLC and the OLC/MnO_2 nanohybrid, (c) galvanostatic charge–discharge curves for the OLC/MnO_2 nanohybrid at various current densities, and (d) C_{sp} *vs.* current densities of the OLC/MnO_2 nanohybrid. Electrolyte: aqueous 1 M Na_2SO_4.

Table 2 Comparison of specific capacitance of various MnO_2-based three-electrode systems

Samples	Electrolyte	C_{sp} (F g^{-1})	i (A g^{-1})	References
Birnessite-type MnO_2	1 M Na_2SO_4	335–408	0.1–0.3	This work
Birnessite-like hollow MnO_2	1 M Na_2SO_4	169	0.25	37
Birnessite-type MnO_2 nanosphere	1 M Na_2SO_4	210	1	38
Birnessite-type MnO_2 nanotube	1 M Na_2SO_4	365	0.25	39
Birnessite-type MnO_2	1 M Na_2SO_4	210	1	40
Birnessite-type MnO_2 nanosheet	1 M Na_2SO_4	269	0.3	41
Birnessite-type MnO_2	1 M Na_2SO_4	~190	0.2	42
Coral-like MnO_2	1 M Na_2SO_4	221	0.5	63
α-MnO_2 ultralong nanowire	0.5 M Na_2SO_4	345	1	64
α-MnO_2 spherical-like particle	1 M Na_2SO_4	259	0.1	65
α-MnO_2 sphere	0.25 M Na_2SO_4	200	1	66
MnO_2 nanosheet	0.1 M Na_2SO_4	182	0.1	67
MnO_2 microsphere	1 M Na_2SO_4	190	0.5	68
MnO_2 nanosheet array	1 M Na_2SO_4	201	1	69
MnO_2 tubular nanostructure	1 M Na_2SO_4	315	0.2	70
Mesoporous MnO_2 particle	1 M Na_2SO_4	173	0.25	71
Porous nano-MnO_2	1 M Na_2SO_4	198	0.28	72
Electrodeposited MnO_2-nanopillars	1 M Na_2SO_4	603	10.0	73

The OLC/MnO_2 is capable of cycling at very high current densities (up to 10 A g^{-1}, Fig. 7d), yielding a high specific capacitance suitable for high power energy storage applications.

Table 3 summarizes the values of the capacitance parameters obtained in comparison with the literature, and it is evident that the OLC/MnO_2 nanohybrid exhibits higher performance (in terms of power density or rate capability) than many state-of-the-art MnO_2-based pseudocapacitors. Note that there has been no known report on symmetric supercapacitors based on birnessite-type MnO_2 in the literature so far; yet, the latter is important to transition to actual devices.

Voltage-holding (or floating) experiments represent a reliable analysis method for establishing the long-term stability of supercapacitor electrodes.[60,61] In this work, the OLC/MnO_2

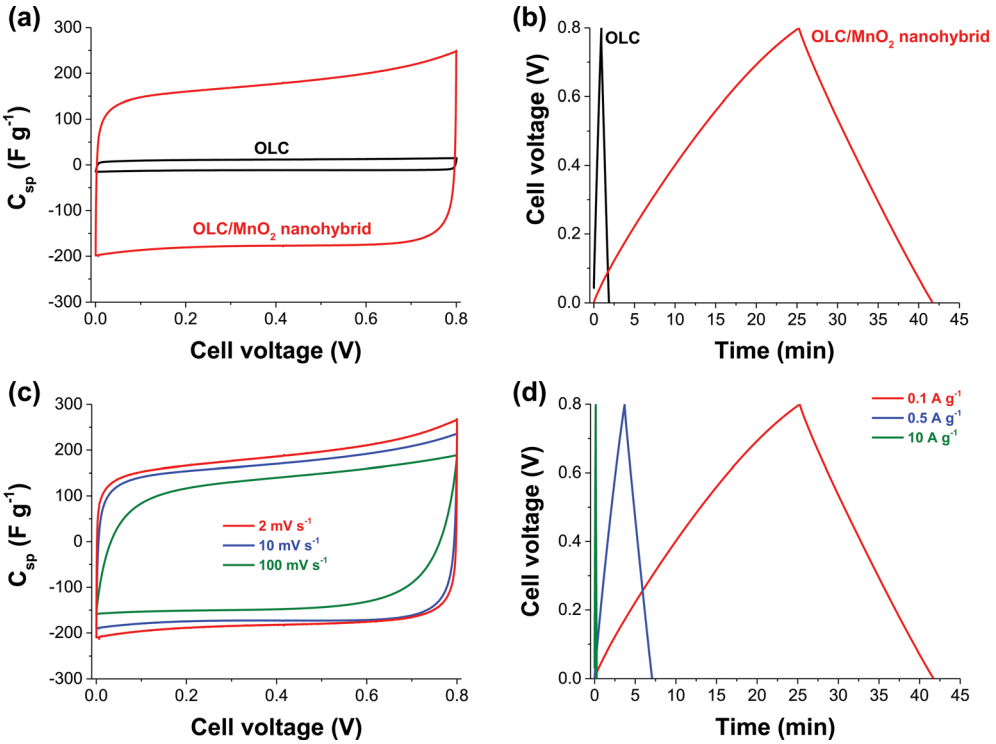

Fig. 7 Nickel foam based 2-electrode (symmetric) configuration: (a) comparative cyclic voltammograms for OLC and OLC/MnO_2 at 5 mV s^{-1}, (b) comparative galvanostatic charge–discharge curves for OLC and OLC/MnO_2 at 0.1 A g^{-1}, (c) CVs at different scan rates for OLC/MnO_2 and (d) comparative galvanostatic charge–discharge curves for OLC and the OLC/MnO_2 nanohybrid at different current densities. Electrolyte: aqueous 1 M Na_2SO_4.

Table 3 Comparison of electrochemical performance of some MnO_2-based aqueous symmetric electrochemical capacitors[a]

Electrode	Electrolyte	V_{max} (V)	C_{sp} (F g^{-1})	E_{sp} (W h kg^{-1})	P_{max} (kW kg^{-1})	#EDR (Ω cm^2)	References
OLC	1 M Na_2SO_4	0.8	12	0.3	2.9	7.8	This work
OLC/MnO_2	1 M Na_2SO_4	0.8	254	5.6	74.8	3.1	This work
GF/MnO_2	1 M Na_2SO_4	1.0	240	8.3	20.0	~11.9	74
C/MnO_2 DNTAs	1 M Na_2SO_4	0.8	161	35.0	16.0	~20	75
CNOs/MnO_2	0.5 M H_2SO_4	1.0	575	30.1	17.9	~7	30
GN-(γ-MnO_2/CNT)	6 M KOH	1.0	310	43.0	26.0	~3.2	76
MnO_2/PDDA/CNO	1 M Na_2SO_4	0.9	219	6.1	—	~8.3	77

[a] Key: GN = graphene nanosheet; GF = graphene foam; CNT = carbon nanotube; DNTA = double-walled nanotube array; CNOs = carbon nano-onions; PDDA: polydiallyldimethylammonium chloride. #The EDR (equivalent distributed resistance) values were obtained prior to stability studies, and were converted to the Ω cm^2 based on the information we extracted from the cited reports.

nanohybrid exhibited excellent stability during voltage-holding over 50 h at 1 A g^{-1} (see ESI, Fig. S4†). This performance has been illustrated by the gradual decrease in the specific capacitance as the current is kept constant at high potential, retaining *ca.* 200 F g^{-1} (*i.e.*, approximately 90% of its initial capacitance of 220 F g^{-1}). The excellent stability of the OLC/MnO_2 nanohybrid showed that this device can be charged and discharged without significant deterioration. These values correspond to a maximum specific energy of 5.6 W h kg^{-1} and an excellent power density of 74.8 kW kg^{-1}. The improved performance of this hybrid symmetric pseudocapacitor is attributed to the combination of the high electrical conductivity of OLC and the highly reversible redox reactions (pseudocapacitance) arising from the nanostructured MnO_2 material.

EIS data were acquired prior to and post-floating experiments for the OLC/MnO_2 nanohybrid material (Fig. 8 and ESI, Fig. S5†) and OLC alone (see ESI, Fig. S6†). The equivalent distributed resistance (EDR), comprising both the equivalent series resistance (ESR) and the ionic resistance within the porous structure (*i.e.*, RC semicircle), was obtained by extrapolating the vertical portion of the plot to the real axis. The OLC/MnO_2 device shows a lower EDR (3.1 Ω cm^2) compared to the OLC alone (7.8 Ω cm^2). However, the RC semicircle for the OLC/MnO_2 is slightly bigger (~1.8 Ω cm^2) than that of the OLC alone (~1.2 Ω cm^2), meaning that the ionic resistance within the porous structure of the pure EDLC (OLC alone) is increased for the OLC/MnO_2 pseudocapacitor. From the Bode plots, the phase angle for the pure OLC is −85° (which is close to the

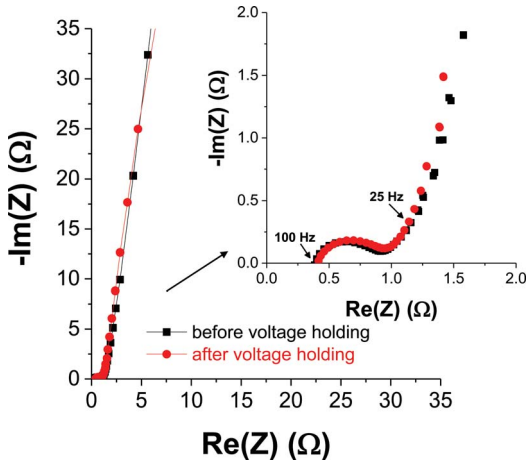

Fig. 8 Nyquist plot for the OLC/MnO_2 symmetric pseudocapacitor before and after 50 h voltage holding experiments. The inset is the expanded portion of the high frequency region. Electrolyte: aqueous 1 M Na_2SO_4.

−90° for an ideal EDLC) compared to the OLC/MnO_2 which is −80°, further indicating the pseudocapacitive behavior of the OLC/MnO_2 device. The knee frequency (f_o, $\phi = -45°$) describes the maximum frequency at which the capacitive behavior is dominant, and is a measure of the power capability of a supercapacitor; the higher the f_o the more rapidly the supercapacitor can be charged and discharged or the higher the power density that can be achieved from the supercapacitor. The values of f_o were *ca.* 25 Hz for the OLC/MnO_2 (time constant ~ 40 ms) and 5 Hz (time constant ~ 0.2 s) for the OLC, which further corroborates the higher power performance of the OLC/MnO_2 over its OLC counterpart. It is important to note that the f_o values remain approximately the same for both devices before and after 50 h voltage holding. This result shows that most of the stored energy in OLC/MnO_2 is accessible up to 25 Hz, that is, the energy output available on the millisecond time scale. It should be stated here that most commercially available supercapacitors, including those designed for higher power applications, operate at frequencies less than 1 Hz.[62]

Conclusions

This work investigated the electrochemical performance of highly graphitized onion-like carbon integrated with nanostructured birnessite-type MnO_2 materials (OLC/MnO_2) when used as a symmetrical pseudocapacitor device. From the half-cell experiment, the OLC/MnO_2 nanohybrid exhibited better performance when using Ni foam as the current collector (in terms of specific capacitance and rate capability) compared to a Pt disc substrate. Based on its excellent performance, Ni foam was used to fabricate the OLC/MnO_2 symmetric pseudocapacitor. The device gave excellent electrochemical performance with a specific capacity of 408 F g^{-1}, specific energy density of 5.6 W h kg^{-1}, power density of 74.8 kW kg^{-1}, capacity retention upon long-hour voltage-holding and cycling, very low equivalent distributed resistance (EDR ≈ 3 Ω cm^2), and very short RC time constant (40 ms). Using such a nanohybrid material, it is possible to overcome the main limitation of MnO_2, namely its poor electrical conductivity (10^{-6} to 10^{-5} S cm^{-1}) and to exploit its main advantages, namely low-cost, high abundance, and environmental friendliness, for high power energy storage devices. Indeed, the electrochemical properties of OLC/MnO_2 nanohybrids as high-rate energy storage devices have great potential for the development of high power aqueous-based supercapacitors that can be deployed for high-power technological applications.

Acknowledgements

This work was funded by the CSIR as well as the South Africa's Department of Science and Technology (DST) and National Research Foundation (NRF) under the "*Nanotechnology Flagship Programme*" (supercapacitors and fuel cell project, Grant no: 69849). KM thanks the DST/NRF for scarce skill doctoral scholarship. PME and KR thank the NRF for postdoctoral fellowships. CSIR, INM, and Saarland University are partners in the CREATe-Network funded by the European Commission. The INM is part of the Leibniz Research Alliance Energy Transition (LVE). The authors acknowledge the funding from the German Federal Ministry for Research and Education (BMBF) in support of the nanoEES^{3D} project (award number 03EK3013) as part of the strategic funding initiative energy storage framework. MZ and VP thank Prof. Eduard Arzt (INM) for his continuous support. Dipl.-Ing. Sebastian Slawik and Prof. Frank Mücklich (Chair of Functional Materials, Saarland University) are thanked for their support regarding X-ray diffraction.

References

1 F. Béguin, V. Presser, a. Balducci and E. Frackowiak, *Adv. Mater.*, 2014, 2219.
2 A. Burke, *J. Power Sources*, 2000, **91**, 37.
3 P. Simon, Y. Gogotsi and B. Dunn, *Science*, 2014, **343**, 1210.
4 V. Augustyn, P. Simon and B. Dunn, *Energy Environ. Sci.*, 2014, **7**, 1597.
5 P. Simon and Y. Gogotsi, *Nat. Mater.*, 2008, **7**, 845.
6 Y. Zhai, Y. Dou, D. Zhao, P. F. Fulvio, R. T. Mayes and S. Dai, *Adv. Mater.*, 2011, **23**, 4828.
7 B. E. Conway, V. Birss and J. Wojtowicz, *J. Power Sources*, 1997, **66**, 1.
8 R. Kotz and M. Carlen, *Electrochim. Acta*, 2000, **45**, 2483.
9 E. Frackowiak and F. Béguin, *Carbon*, 2001, **39**, 937.
10 J. R. Miller, *Science*, 2012, **335**, 1312.
11 C. Largeot, C. Portet, J. Chmiola, P. Taberna, Y. Gogotsi and P. Simon, *J. Am. Chem. Soc.*, 2008, **130**, 2730.
12 E. Frackowiak, *Phys. Chem. Chem. Phys.*, 2007, **9**, 1774.
13 A. T. Chidembo, K. I. Ozoemena, B. O. Agboola, V. Gupta, G. G. Wildgoose and R. G. Compton, *Energy Environ. Sci.*, 2010, **3**, 228.
14 A. Bello, K. Makgopa, M. Fabiane, D. Dodoo-Ahrin, K. I. Ozoemena and N. Manyala, *J. Mater. Sci.*, 2013, **48**, 6707.

15 C. J. Jafta, F. Nkosi, L. le Roux, M. K. Mathe, M. Kebede, K. Makgopa, Y. Song, D. Tong, M. Oyama, N. Manyala, S. Chen and K. I. Ozoemena, *Electrochim. Acta*, 2013, 2.
16 E. J. Ra, E. Raymundo-Piñero, Y. H. Lee and F. Béguin, *Carbon*, 2009, **47**, 2984.
17 J. Li, E. Liu, W. Li, X. Meng and S. Tan, *J. Alloys Compd.*, 2009, **478**, 371.
18 U. Fischer, R. Saliger and V. Bock, *J. Porous Mater.*, 1997, **285**, 281.
19 Y. Wang, Z. J. Han, S. F. Yu, R. R. Song, H. H. Song, K. Ken Ostrikov and H. Y. Yang, *Carbon*, 2013, **64**, 230.
20 Y. Wang, F. Yan, S. W. Liu, A. Y. S. Tan, H. Song, X. W. Sun and H. Y. Yang, *J. Mater. Chem. A*, 2013, **1**, 5212.
21 D. M. Anjos, J. K. McDonough, E. Perre, G. M. Brown, S. H. Overbury, Y. Gogotsi and V. Presser, *Nano Energy*, 2013, **2**, 702.
22 I. Kovalenko, D. G. Bucknall and G. Yushin, *Adv. Funct. Mater.*, 2010, **20**, 3979.
23 Y. Gao, Y. S. Zhou, M. Qian, X. N. He, J. Redepenning, P. Goodman, H. M. Li, L. Jiang and Y. F. Lu, *Carbon*, 2013, **51**, 52.
24 E. G. Bushueva, P. S. Galkin, A. V. Okotrub, L. G. Bulusheva, N. N. Gavrilov, V. L. Kuznetsov and S. I. Moiseekov, *Phys. Status Solidi*, 2008, **245**, 2296.
25 C. Portet, G. Yushin and Y. Gogotsi, *Carbon*, 2007, **45**, 2511.
26 J. K. McDonough, A. I. Frolov, V. Presser, J. Niu, C. H. Miller, T. Ubieto, M. V. Fedorov and Y. Gogotsi, *Carbon*, 2012, **50**, 3298.
27 I. Suarez-Martinez, N. Grobert and C. P. Ewels, *Carbon*, 2012, **50**, 741.
28 V. N. Mochalin, O. Shenderova, D. Ho and Y. Gogotsi, *Nat. Nanotechnol.*, 2012, **7**, 11.
29 D. Pech, M. Brunet, H. Durou, P. Huang, V. Mochalin, Y. Gogotsi, P.-L. Taberna and P. Simon, *Nat. Nanotechnol.*, 2010, **5**, 651.
30 M. V. K. Azhagan, M. V. Vaishampayan and M. V. Shelke, *J. Mater. Chem. A*, 2014, **2**, 2152.
31 V. L. Kuznetsov, A. L. Chuvilin, Y. V. Butenko, I. Y. Mal'kov and V. M. Titov, *Chem. Phys. Lett.*, 1994, **222**, 343.
32 D. Urgate, *Nature*, 1992, **359**, 707.
33 S. Iijima, *J. Cryst. Growth*, 1980, **50**, 675.
34 M. Choucair and J. A. Stride, *Carbon*, 2012, **50**, 1109.
35 C. Julien, *Solid State Ionics*, 2003, **159**, 345.
36 C. Matei Ghimbeu, A. Malak-Polaczyk, E. Frackowiak and C. Vix-Guterl, *J. Appl. Electrochem.*, 2013, **44**, 123.
37 P. Yu, X. Zhang, Y. Chen and Y. Ma, *Mater. Lett.*, 2010, **64**, 1480.
38 B. Ming, J. Li, F. Kang, G. Pang, Y. Zhang, L. Chen, J. Xu and X. Wang, *J. Power Sources*, 2012, **198**, 428.
39 M. Huang, Y. Zhang, F. Li, L. Zhang, R. S. Ruoff, Z. Wen and Q. Liu, *Sci. Rep.*, 2014, **4**, 3878.
40 X. Zhang, X. Sun, H. Zhang, D. Zhang and Y. Ma, *Mater. Chem. Phys.*, 2012, **137**, 290.
41 X. Zhang, P. Yu, H. Zhang, D. Zhang, X. Sun and Y. Ma, *Electrochim. Acta*, 2013, **89**, 523.
42 Y. Wang, S. F. Yu, C. Y. Sun, T. J. Zhu and H. Y. Yang, *J. Mater. Chem.*, 2012, **22**, 17584.
43 P. Yang, Y. Ding, Z. Lin, Z. Chen, Y. Li, P. Qiang, M. Ebrahimi, W. Mai, C. P. Wong and Z. L. Wang, *Nano Lett.*, 2014, **14**, 731.
44 Z.-S. Wu, W. Ren, D.-W. Wang, F. Li, B. Liu and H.-M. Cheng, *ACS Nano*, 2010, **4**, 5835.
45 H. Xia, Y. Wang, J. Lin and L. Lu, *Nanoscale Res. Lett.*, 2012, **7**, 33.
46 H. Yang, J. Jiang, W. Zhou, L. Lai, L. Xi, Y. M. Lam, Z. Shen, B. Khezri and T. Yu, *Nanoscale Res. Lett.*, 2011, **6**, 531.
47 D. Weingarth, M. Zeiger, N. Jäckel, M. Aslan, G. Feng and V. Presser, *Adv. Energy Mater.*, 2014, **4**, 1400316.
48 S. Brunauer, P. H. Emmett and E. Teller, *J. Am. Chem. Soc.*, 1938, **60**, 309.
49 G. Y. Gor, M. Thommes, K. A. Cychosz and A. V. Neimark, *Carbon*, 2012, **50**, 1583.
50 Y. V. Butenko, V. L. Kuznetsov, A. L. Chuvilin, V. N. Kolomiichuk, S. V. Stankus, R. A. Khairulin and B. Segall, *J. Appl. Phys.*, 2000, **88**, 4380.
51 T. K. Gupta, B. P. Singh, V. N. Singh, S. Teotia, A. P. Singh, I. Elizabeth, S. R. Dhakate, S. K. Dhawan and R. B. Mathur, *J. Mater. Chem. A*, 2014, **2**, 4256.
52 K. Bogdanov, A. Fedorov, V. Osipov, T. Enoki, K. Takai, T. Hayashi, V. Ermakov, S. Moshkalev and A. Baranov, *Carbon*, 2014, **73**, 78.
53 D. Yang and M. Wang, *Chem. Mater.*, 2001, **13**, 2589.
54 F.-J. Liu, *J. Power Sources*, 2008, **182**, 383.
55 Z. Li, Y. Mi, X. Liu, S. Liu, S. Yang and J. Wang, *J. Mater. Chem.*, 2011, **21**, 14706.
56 Y.-K. Hsu, Y.-C. Chen, Y.-G. Lin, L.-C. Chen and K.-H. Chen, *J. Mater. Chem.*, 2012, **22**, 2733.
57 M. C. Biesinger, B. P. Payne, A. P. Grosvenor, L. W. M. Lau, A. R. Gerson and R. S. C. Smart, *Appl. Surf. Sci.*, 2011, **257**, 2717.
58 T. E. Rufford, D. Hulicova-Jurcakova, K. Khosla, Z. Zhu and G. Q. Lu, *J. Power Sources*, 2010, **195**, 912.
59 L.-Y. Lin, M.-H. Yeh, J.-T. Tsai, Y.-H. Huang, C.-L. Sun and K.-C. Ho, *J. Mater. Chem. A*, 2013, **1**, 11237.
60 D. Weingarth, A. Foelske-Schmitz and R. Kötz, *J. Power Sources*, 2013, **225**, 84.
61 P. Ratajczak, K. Jurewicz and F. Béguin, *J. Appl. Electrochem.*, 2013, **44**, 475.
62 J. R. Miller, *Electrochem. Soc. Proc. Ser.*, 1996, 246, PV95-29.
63 Y. Zhao, P. Jiang and S.-S. Xie, *J. Power Sources*, 2013, **239**, 393.
64 W. Li, Q. Liu, Y. Sun, J. Sun, R. Zou, G. Li, X. Hu, G. Song, G. Ma, J. Yang, Z. Chen and J. Hu, *J. Mater. Chem.*, 2012, **22**, 14864.
65 Y. Zhang, G. Li, Y. Lv, L. Wang, A. Zhang, Y. Song and B. Huang, *Int. J. Hydrogen Energy*, 2011, **36**, 11760.
66 Y. Zhang, C. Sun, P. Lu, K. Li, S. Song and D. Xue, *CrystEngComm*, 2012, **14**, 5892.
67 H. Jang, S. Suzuki and M. Miyayama, *J. Electrochem. Soc.*, 2012, **159**, A1425.
68 W. Ko, L. Chen, Y. Chen, W. Chen, K. Lu, J. Yang, Y. Yen and K. Lin, *J. Phys. Chem. C*, 2013, **117**, 16290.
69 M. Kundu and L. Liu, *J. Power Sources*, 2013, **243**, 676.

70 J. Zhu, W. Shi, N. Xiao, X. Rui, H. Tan, X. Lu, H. H. Hng, J. Ma and Q. Yan, *ACS Appl. Mater. Interfaces*, 2012, **4**, 2769.
71 L. Chen, N. Gu, R. Ding, L. Qi and H. Wang, *J. Solid State Electrochem.*, 2013, **17**, 2579.
72 H.-Q. Wang, G. Yang, Q.-Y. Li, X.-X. Zhong, F.-P. Wang, Z.-S. Li and Y. Li, *New J. Chem.*, 2011, **35**, 469.
73 Z. Yu, B. Duong, D. Abbitt and J. Thomas, *Adv. Mater.*, 2013, **25**, 3302.
74 A. Bello, O. O. Fashedemi, J. N. Lekitima, M. Fabiane, D. Dodoo-Arhin, K. I. Ozoemena, Y. Gogotsi, A. T. Charlie Johnson and N. Manyala, *AIP Adv.*, 2013, **3**, 082118.
75 Q. Li, X.-F. Lu, H. Xu, Y.-X. Tong and G.-R. Li, *ACS Appl. Mater. Interfaces*, 2014, **6**, 2726.
76 R. B. Rakhi, W. Chen, D. Cha and H. N. Alshareef, *Adv. Energy Mater.*, 2012, **2**, 381.
77 R. Borgohain, J. P. Selegue and Y.-T. Cheng, *J. Mater. Chem. A*, 2014, **2**, 20367.